RSC Advances

PAPER

View Article Online
View Journal | View Issue

Cite this: *RSC Adv.*, 2025, **15**, 27154

Study on morphological, FTIR, optical band-gap and AC conductivity of $Li_2CoP_2O_7$ for advanced applications

Samia Aydi,[a] Amar Djemli,[b] Obaidallah A. Algethami,[c] Sami Znaidia,[d] Foudil Sahnoune[b] and Abderrazek Oueslati *[a]

Lithium diphosphates, and particularly $Li_2CoP_2O_7$, have garnered increasing attention due to their promising properties for applications in energy storage and electronic devices. In the present study, $Li_2CoP_2O_7$ was successfully synthesized using a conventional solid-state reaction route. X-ray powder diffraction (XRD) analysis confirmed the formation of a pure monoclinic phase with *C*2/*c* space group symmetry and an average grain size of approximately 2.66 μm. Infrared (IR) spectroscopy revealed distinct vibrational modes characteristic of $P_2O_7^{4-}$ groups, in line with the expected structural framework. Optical absorption measurements indicated that the material exhibits semiconducting behavior, with an estimated indirect band gap of approximately 3.78 eV. Dielectric studies demonstrated that $Li_2CoP_2O_7$ possesses excellent dielectric performance, including a remarkably high dielectric constant ($\sim 2 \times 10^8$), suggesting its suitability for low-frequency energy storage applications. Impedance spectroscopy measurements revealed a non-Debye relaxation mechanism, with temperature-dependent relaxation dynamics analyzed using the Arrhenius model. Furthermore, the frequency-dependent ac conductivity followed Jonscher's universal power law, and the behavior of the frequency exponent s was consistent with the correlated barrier hopping (CBH) conduction model. Overall, these findings offer valuable insights into the dielectric relaxation processes and charge transport mechanisms in $Li_2CoP_2O_7$, underscoring its potential for high-performance applications in advanced electronic systems and energy storage technologies.

Received 10th June 2025
Accepted 16th July 2025

DOI: 10.1039/d5ra04105h

rsc.li/rsc-advances

1. Introduction

Diphosphates have gained significant research interest due to their stable structure, which features high permittivity, a large number of storage sites, wide channels for electrolyte ion movement, and the multiple valency of phosphorus.[1–8] These characteristics make diphosphates ideal materials for a variety of technological applications, including in medical fields, battery cathode materials, optoelectronic devices, catalysts, ionic conductors, lasers, pigments, and magnetic refrigeration.[9–11] In this regard, lithium metal phosphate materials, represented by the formula $Li_2MP_2O_7$ (where M = Ba, Ni, Zn, Cu, *etc.*), belong to the broad family of $A_2MP_2O_7$ compounds. These materials are defined by the simultaneous presence of an alkali metal ion (A^+) and a divalent cation (M^{2+}). Among this group, several compounds have been extensively studied for their electrical and dielectric properties. Specifically, $Li_2FeP_2O_7$, $Li_2NiP_2O_7$, $Li_2CuP_2O_7$, and $Li_2BaP_2O_7$ have garnered significant attention in the literature.[12–15] These materials are considered promising for a range of applications due to their distinct electrochemical properties, which has led to increased research into their potential use in energy storage and related technologies. Lithium cobalt diphosphate ($Li_2CoP_2O_7$) is a notable compound within this group, attracting significant attention due to its remarkable structural and physical properties. These include luminescence, dielectric, semiconductor, catalytic, magnetic, fluorescent, and ion-exchange capabilities.[16–21] Furthermore, $Li_2CoP_2O_7$ exhibits high structural stability, attributed to the strong P–O covalent bonds, making it an environmentally cost-effective material.[22–26] Extensive studies have been undertaken on compounds with the general formula $Li_2MP_2O_7$, encompassing $Li_2CoP_2O_7$, as part of thorough investigations into these materials.[27] At room temperature, the crystal structure of Lithium cobalt diphosphate is characterized by a monoclinic system with a *C*2/*c* space group. The structural framework consists of CoO_6 polyhedra linked by edges to the $P_2O_7^{4-}$ units. Despite its potential, the electrical and dielectric properties of

[a]*Laboratory of Spectroscopic Characterization and Optics of Materials, Faculty of Sciences, University of Sfax, B. P. 1171, 3000 Sfax, Tunisia. E-mail: oueslatiabderrazek@yahoo.fr*

[b]*Department of Physics, University Mohamed Boudiaf of M'sila, 28000, M'sila, Algeria*

[c]*Departement of Physics, Faculty of Science, Al-Baha University, Alaqiq, 65779, Saudi Arabia*

[d]*Department of Physics, Faculty of Science, King Khalid University, Abha, Saudi Arabia*

lithium cobalt pyrophosphate have not been thoroughly explored. This research aims to provide a deeper understanding of how temperature and frequency influence conductivity, with the goal of uncovering the underlying conduction mechanisms and identifying potential applications for its distinctive electrical characteristics. Given the foregoing, we conduct an in-depth examination of the morphological, optical, dielectric, and electrical properties of our ceramic, focusing on parameters such as permittivity, AC conductivity, DC conductivity, and its activation energy across a broad spectrum of frequencies and temperatures. Various models are employed to elucidate the AC conduction mechanism through fitting, revealing the presence of sublinear behavior (including the single Jonscher law), superlinear behavior, high-frequency plateaus, and dielectric relaxation processes in the prepared ceramic material.

2. Experimental

The $Li_2CoP_2O_7$ material was synthesized using a solid-state reaction method. All reagents used were of analytical grade and did not undergo any additional treatment. Stoichiometric quantities of lithium carbonate (Li_2CO_3, ≥ 99%, Sigma-Aldrich), cobalt(II) oxide (CoO, ≥ 99%, Sigma-Aldrich), and ammonium dihydrogen phosphate ($NH_4H_2PO_4$, ≥ 99%, Sigma-Aldrich) were thoroughly mixed by grinding in an agate mortar for two hours. The resulting mixture was then heated for six hours at 623 K to eliminate ammonia, water, and carbon dioxide. After re-grinding, the powder was compacted into pellets with a diameter of 8 mm and a thickness of 1.2 mm. These pellets were sintered in air at 923 K for six hours to produce the ceramic $Li_2CoP_2O_7$.

An analysis of the sample's crystal structure was conducted using a PANalytical X'Pert Pro X-ray diffractometer with CuKα radiation ($\lambda = 1.5418$ Å) over a broad range of Bragg angles ($10 \leq 2\theta \leq 60°$). The scan was performed with a step size of 0.02° and a scan rate of 0.02° per s to ensure high-resolution data acquisition. The structural parameters were determined by fitting the experimental XRD data using the Rietveld refinement method with FULLPROF software.[28]

To confirm the uniformity and chemical composition of the compound, high-resolution images were captured using a JEOL JSM-IT200 scanning electron microscope, which was fitted with an Oxford Inca Energy X-ray detector for energy-dispersive spectroscopy (EDS) analysis.

Infrared spectroscopy was performed on a PerkinElmer FTIR-100 spectrophotometer over the wavenumber range of 400–1200 cm^{-1}. The optical properties were assessed through photoluminescence analysis at room temperature using a Shimadzu UV-3101PC spectrophotometer, scanning wavelengths from 400 to 800 nm. Electrical measurements were conducted on a pellet sample (8 mm in diameter and 1.2 mm thick) with silver electrodes attached to both sides. The measurements were taken over a frequency range of 10 Hz to 10^7 Hz at temperatures between 413 K and 573 K using a Solartron impedance analyzer within a temperature-controlled setup.

3. Data analysis and discussion

3.1. X-ray diffraction analysis

The X-ray diffraction (XRD) pattern of $Li_2CoP_2O_7$ powder recorded at room temperature is presented in Fig. 1(a). The well-defined diffraction peaks are characteristic of a pyrophosphate-type structure, indicating successful phase formation. The absence of secondary phases or additional peaks suggests that the synthesized compound is highly crystalline and phase-pure. Rietveld refinement of the XRD data was performed using the FullProof suite to determine precise structural parameters and further validate phase purity. The close agreement between the observed and calculated patterns confirms that $Li_2CoP_2O_7$ crystallizes in a monoclinic structure, belonging to the $C2/c$ space group, which is isomorphic to $Li_2NiP_2O_7$.[29] In addition, the most intense diffraction peaks have been indexed with their corresponding (hkl) planes to facilitate phase identification and structural analysis. The refined lattice parameters, detailed in Table 1, closely match those calculated from the JCPDS reference 85-0002.[30]

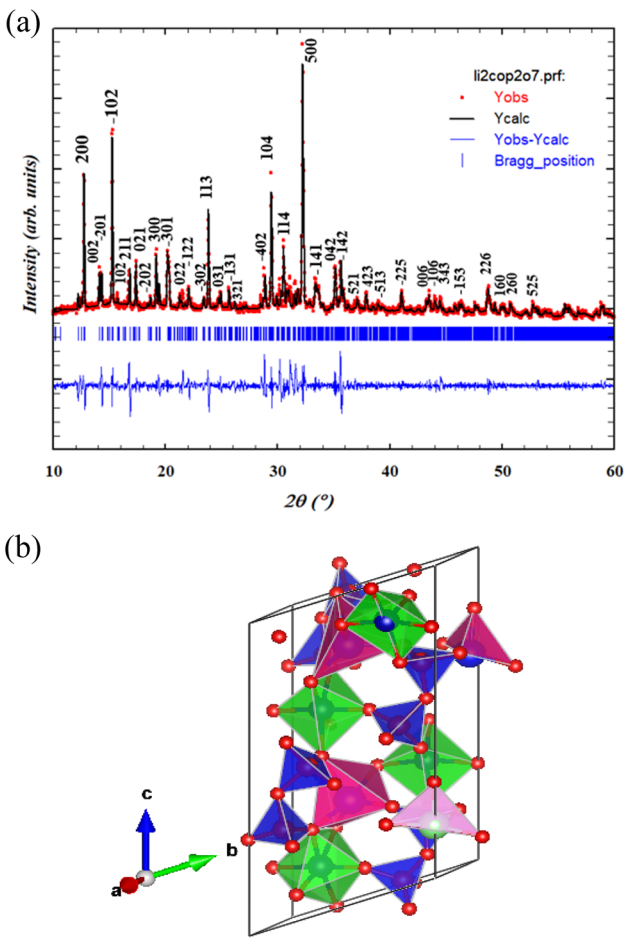

Fig. 1 (a) Rietveld refinement profile carried out through full proof software of $Li_2CoP_2O_7$. (b) Crystal structure of $Li_2CoP_2O_7$.

Table 1 Crystallographic data of the structure refinement of $Li_2CoP_2O_7$ at room temperature

Compound	$Li_2CoP_2O_7$
Space group	*C*2/*c*
Crystal system	Monoclinic
a (Å)	14.3609 (5)
b (Å)	11.2058 (5)
c (Å)	13.6451 (5)
R_p	9.36
R_{wp}	7.40
R_{exp}	6.90
Density (g cm^{-3})	3.43
Porosity%	6.5
Atom	Li, Co, P, O
Wyckoff position	4a, 4b, 8d, 16e
Atomic%	13.33, 6.67, 26.67, 53.33
Average bond length (Å)	Li–O 2.02
	Co–O 2.06
	P–O 1.52
Bond angles (°)	O–Li–O: 104
	O–Co–O: 89
	O–P–O: 107
Coordination environment	LiO_4 tetrahedron
	CoO_6 octahedron
	PO_4 tetrahedron

Indeed, the schematic crystal structure of $Li_2CoP_2O_7$ is illustrated in Fig. 1(b). The crystal structure features a three-dimensional framework composed of intersecting tunnels aligned along the [001] and [110] crystallographic directions, with Li^+ ions situated at the intersections of these channels. These tunnels, along with the associated voids, provide viable pathways for Li^+ ion mobility and create favorable sites for the intercalation of guest cations. The structural backbone is constructed from corner-sharing CoO_6 octahedra and P_2O_7 groups, contributing to the overall rigidity and connectivity of the lattice. Detailed crystallographic parameters, including the Wyckoff positions, atomic percentages, theoretical density, porosity, average bond lengths, and bond angles, are presented in Table 1.

Additionally, the XRD pattern is used to calculate the average crystallite size and microstrain (ε) for the $Li_2CoP_2O_7$ sample. In the context of X-ray diffraction, the Scherrer equation is used to estimate the size of crystallites based on the broadening of diffraction peaks. This method assumes that peak broadening is solely due to crystallite size, but in reality, other factors like microstrain can contribute to broader peaks. The average crystallite size (D_{SC}) is determined using the Debye–Scherrer equation, as explained in:[31]

$$D_{SC} = \frac{K\lambda}{\beta \cos\theta} \quad (1)$$

The Scherrer equation involves parameters such as the shape factor K, typically around 0.9, the X-ray wavelength λ, the full width at half maximum (FWHM) β in radians, and Bragg's angle θ in degrees. However, the presence of microstrain can lead to an overestimation of crystallite size, as it increases the peak width. Microstrain ε is estimated using a separate equation, which helps account for these additional effects on peak broadening:[32]

$$\varepsilon = \frac{\beta}{4 \tan\theta} \quad (2)$$

The calculated parameters D_{SC} and ε were found to be 35 nm and 4×10^{-3}, respectively. The material's porosity was calculated to be 6.5%, indicating the presence of voids within its structure. Generally, lower porosity values are preferred because they enhance electrical properties. The porosity can be determined using a specific equation, as described in reference:[33]

$$P\ (\%) = \left(1 - \frac{D_{Th}}{D_{exp}}\right) \times 100 \quad (3)$$

The material exhibited an X-ray density (D_{exp}) of 3.41 g cm^{-3} and a bulk density (D_{Th}) of 3.2 g cm^{-3}. A dislocation density of 4.0×10^1 cm^{-2} was derived from calculations, indicating a low concentration of crystalline defects. Such reduced defect levels are advantageous for maintaining the material's structural stability and functional efficiency. The determination of dislocation density was performed using the methodology outlined in reference:[33]

$$\delta = \frac{1}{D_{SC}} \quad (4)$$

The interplay among these calculated parameters are significant for comprehending the material's behavior and performance. This material with low porosity and dislocation density typically exhibits a well-structured form with fewer defects, which enhances its dielectric and electrical properties. This relationship highlights the suitability of the $Li_2CoP_2O_7$ compound for low-frequency electronic applications, show casing its potential for advanced technological.[34]

3.2. SEM/EDS analysis

Prior to crystal structure analysis, a micrograph was obtained to evaluate the material's homogeneity and surface morphology. The SEM micrographs in Fig. 2(a) and (b), captured at 2 μm and 5 μm scales, demonstrate the synthesized material's highly compact structure with uniformly distributed grains. Observations reveal hexagonal geometries, angular particles of varying sizes, and porous regions, alongside a clustering tendency among particles that may influence electrical behavior. Grain size analysis *via* ImageJ software,[35] employing Lorentzian curve fitting (Fig. 2(c)), yields an average dimension of 2.66 μm. This value significantly exceeds estimates derived from Scherrer's equation, suggesting that individual particles imaged *via* SEM represent aggregates of smaller crystalline domains. The larger apparent grain size implies reduced grain boundary density, a feature beneficial for energy storage systems as it minimizes ion transport barriers and improves structural integrity.[36]

Fig. 3 displays the EDX spectra of the $Li_2CoP_2O_7$ compound, exhibiting distinct peaks corresponding to cobalt (Co), phosphorus (P), and oxygen (O), with no extraneous elements

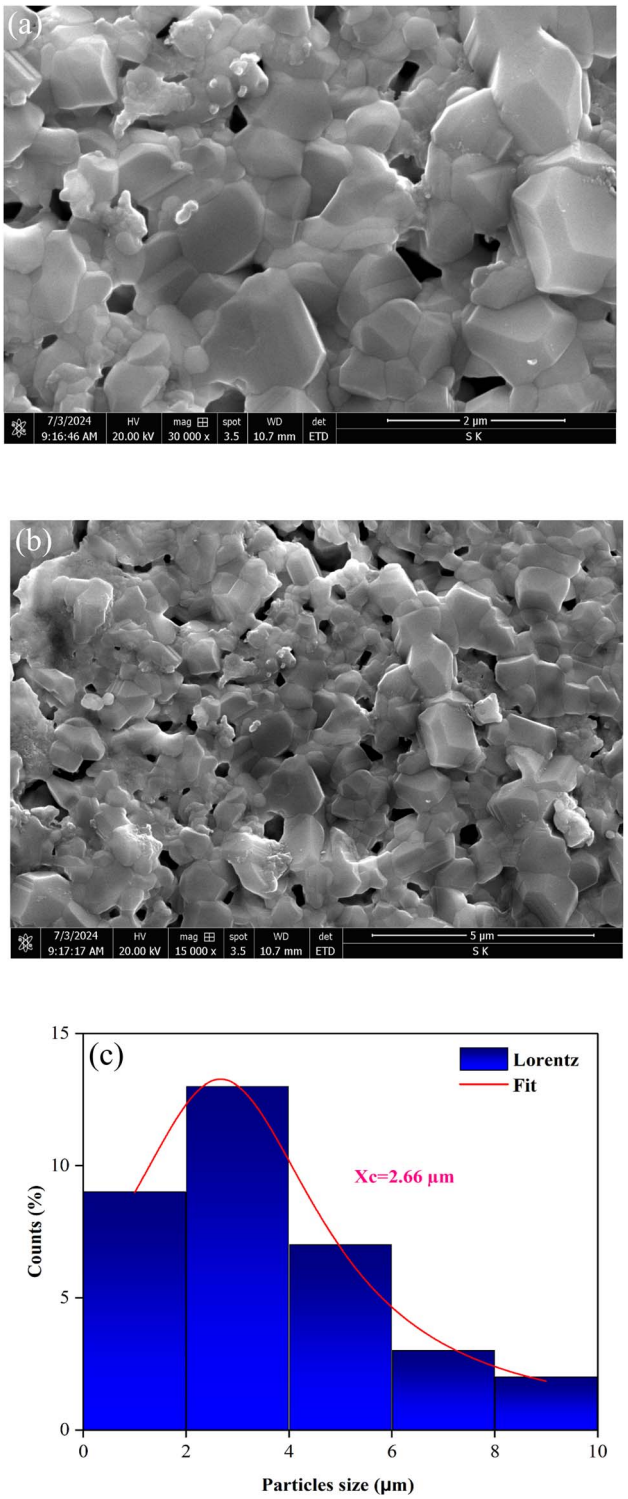

Fig. 2 (a) SEM image of $Li_2CoP_2O_7$. (b) SEM image of $Li_2CoP_2O_7$. (c): The corresponding average particle size histogram of $Li_2CoP_2O_7$.

detected, confirming compositional purity. The absence of lithium (Li) signals in the spectrum is attributed to its low atomic number, which lies below the detection sensitivity threshold of EDX. The strong concordance between XRD and EDX results reinforces the reliability of the structural and compositional data.

Table 2 compares the experimentally determined atomic weight percentages with the theoretical stoichiometric composition of the compound, showing excellent agreement and indicating no elemental loss during synthesis. Semi-quantitative EDS analysis, conducted on a specific cross-sectional region of the SEM micrograph (Fig. 4(a–e)), further validates the homogeneous spatial distribution of Co, P, and O throughout the sample.

3.3. FTIR spectroscopy

The FTIR spectrum of the compound currently being examined is presented in Fig. 5. The vibrational features observed in the wavenumber range (400–1200 cm^{-1}) resemble those of the $P_2O_7^{4-}$ group reported in ref. 37. For the pyrophosphate anion ($P_2O_7^{4-}$), four primary vibrational modes are observed:

*Symmetric P–O stretching (ν_1, A_1 symmetry) at 949 cm^{-1}.

*Antisymmetric P–O stretching (ν_3, T_2 symmetry) at 1035 cm^{-1}.

*Symmetric O–P–O bending (ν_2, E symmetry) at 590 cm^{-1}.

*Antisymmetric O–P–O bending (ν_4, T_2 symmetry) at 637 cm^{-1}.

The bands at 1150 cm^{-1} and 1088 cm^{-1} correspond to overlapping symmetric and antisymmetric vibrational modes of the $P_2O_7^{4-}$ group. These spectral features confirm the presence of distinct stretching and bending motions within the pyrophosphate structural units.

3.4. Optical properties

To investigate the semiconducting properties of our prepared sample, we performed a solid-state UV-vis spectroscopy analysis, examining the absorption coefficient and reflectance spectrum of the compound across a wavelength range of 400–800 nm at room temperature, as illustrated in Fig. 6(a). Four distinct absorption bands were observed at 475, 500, 550, and 750 nm. The bands at 550 and 750 nm are associated with electronic transitions within the $[P_2O_7]$ ion, involving charge transfer from oxygen atoms to the central phosphate atom. In contrast, the bands at 475 and 500 nm are attributed to transitions related to lithium and cobalt ions.

To determine the band gap energy, we employed the Tauc model, which is given by the equation.[38]

$$\alpha h\nu = (h\nu - E_g)^n \quad (5)$$

The absorption coefficient (α), Planck's constant (h), and photon frequency (ν) are key components in determining the optical band gap (E_g). The exponent n can take values of 1/2 and 2, corresponding to direct and indirect allowed transition band gaps, respectively. The Tauc plot for $Li_2CoP_2O_7$ ceramic, as shown in Fig. 6(b), allows the determination of the optical band gap by extrapolating the linear portion of the curves to intersect with the photon energy ($h\nu$). The optical band gap of $Li_2CoP_2O_7$ was estimated to be approximately 3.78 eV assuming an indirect electronic transition, and 4.68 eV for a direct transition, based on Tauc plot analysis. These results confirm that $Li_2CoP_2O_7$ behaves as an indirect band gap semiconductor. The relatively

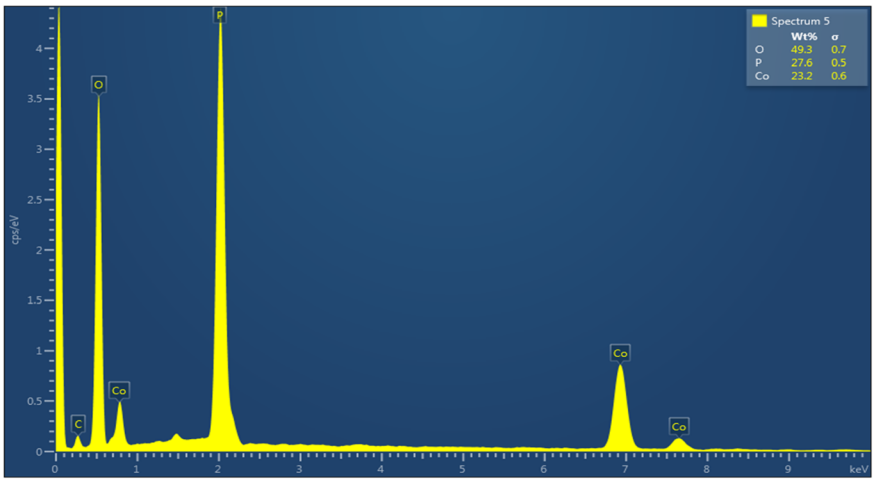

Fig. 3 EDX spectrum of the fractured surface of $Li_2CoP_2O_7$.

Table 2 Atomic ratio of the detected elements of $Li_2CoP_2O_7$

Element	Theoretical at%	Experimental at%	Theoretical wt%	Experimental wt%
Li	16.67	—	5.62	—
Co	8.33	21.5%	23.89	32.2
P	16.67	27.6%	25.10	27.6
O	58.33	49.3%	45.39	40.2

wide band gap highlights its potential for use in optoelectronic applications, particularly those operating in the ultraviolet (UV) region such as UV photodetectors, optical filters, and insulating layers. Furthermore, the large band gap implies a low intrinsic carrier concentration at ambient temperature, which is beneficial for minimizing leakage currents in electronic devices, thereby enhancing their performance and stability, particularly when compared to other diphosphates like $KCrP_2O_7$.[39]

The Urbach energy, a crucial parameter in solid-state physics, characterizes the exponential absorption edge in semiconductors and insulators. This energy is usually calculated using a particular formula:[40]

$$\alpha = \alpha_0 \exp\left(\frac{h\nu - E_g}{E_u}\right) \quad (6)$$

In this equation, α_0 is a constant and E_u represents the Urbach energy in electronvolts (eV). By applying the natural logarithm to both sides of eqn (6), we can derive the following relationship:

$$\mathrm{Ln}(\alpha) = \ln(\alpha_0) + \frac{h\nu}{E_u} \quad (7)$$

The Urbach energy can be determined by plotting the natural logarithm of the absorption coefficient ($\ln(\alpha)$) against photon energy ($h\nu$). The calculation involves taking the reciprocal of the slope of the linear segment of this plot. Our analysis revealed that the band gap energy is approximately 13% of the Urbach energy (E_u), which is 0.29 eV.

Additional key optical properties relevant to our sample include the refractive index (R.I) and metallization criteria (M). The refractive index (n) of the prepared material was determined using an expression based on its optical energy band gap:[41]

$$\frac{n^2-1}{n^2+1} = 1 - \frac{\sqrt{E_g}}{20} \quad (8)$$

The calculated refractive index (n) is 4.42, obtained using eqn (8). The metallization criteria (M) quality is evaluated using the eqn (9), which reflects how the material behaves in terms of optical properties and potential metallic characteristics:[42]

$$M = 1 - \frac{n^2-1}{n^2+1} \times \frac{\sqrt{E_g}}{20} \quad (9)$$

The substance is classified as non-metallic if its M value is less than 1, and metallic if the M value exceeds 1.30. Given that the calculated M value is 0.91, it confirms that the prepared diphosphate is non-metallic in nature, which aligns with its semi-conducting properties.

3.5. Dielectric analysis

In recent years, significant attention has been devoted to investigating the dielectric properties of $Li_2CoP_2O_7$ pyrophosphate materials.[43–46] It has been established that their dielectric behavior is governed by several factors, such as electrode

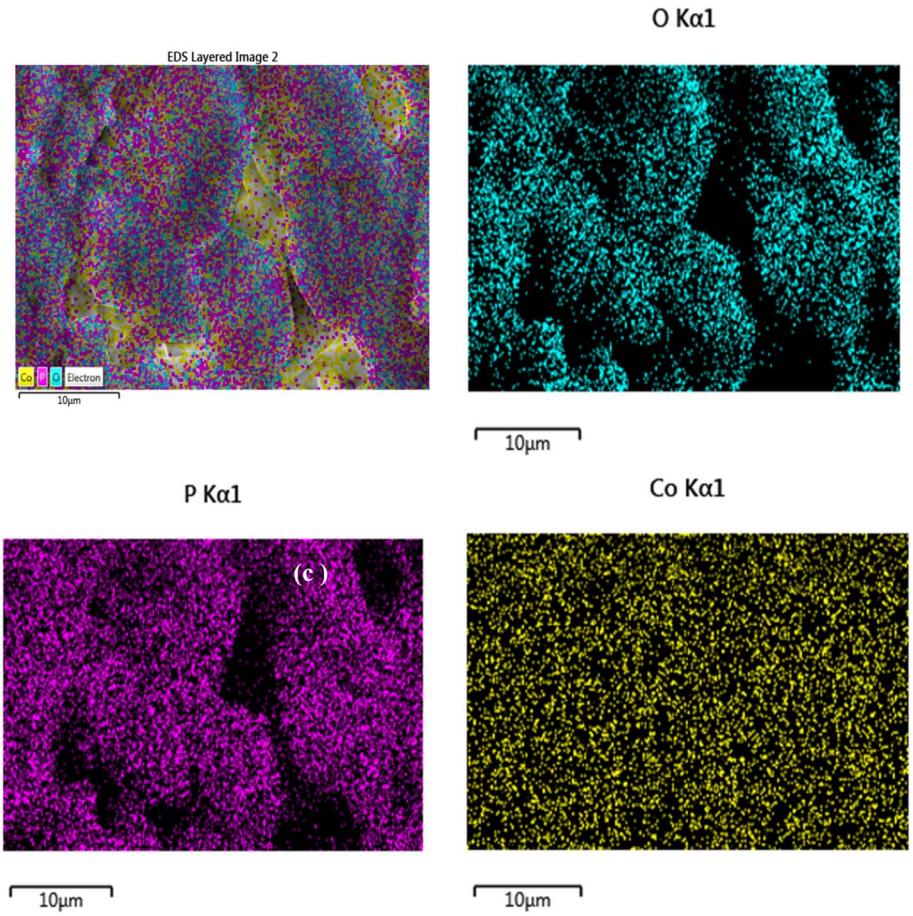

Fig. 4 The EDS element mappings of (CO, P, O) and Co, P, O.

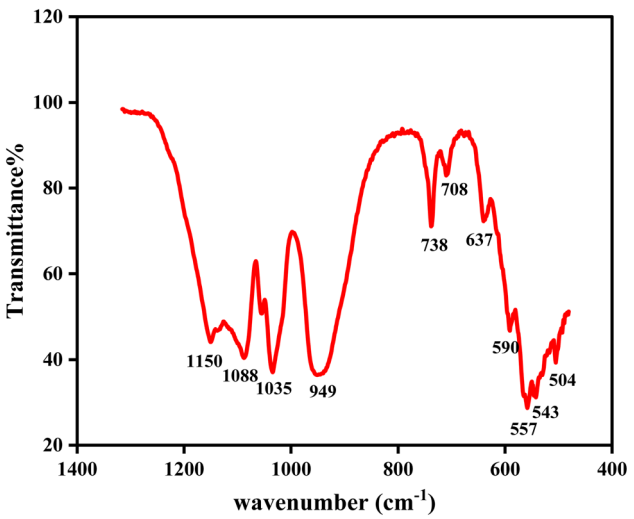

Fig. 5 The FTIR spectrum of $Li_2CoP_2O_7$ compound.

material interface effects, inhomogeneities in the ceramic microstructure, the presence of structural defects, polarization mechanisms associated with polaron hopping, variable oxidation states of transition metal ions, and the spatial distribution of ionic species within the lattice.[47] In this work, the dielectric behavior of the synthesized $Li_2CoP_2O_7$ ceramic is systematically examined, with a focus on how changes in frequency and temperature affect both the real (ε') and imaginary (ε'') parts of the dielectric permittivity.

Fig. 7(a) illustrates how the real part of the dielectric constant, ε', changes as a function of angular frequency. The dielectric properties of the material were studied over a temperature range of 413–673 K, with an analysis of their frequency dependence. The real part of the dielectric permittivity (ε') of the $Li_2CoP_2O_7$ compound exhibits significantly high values, reaching up to 2×10^8 at low frequencies (Fig. 7(a)). This pronounced increase in ε' at low frequencies is typically associated with space charge polarization, particularly at grain boundaries. The accumulation of charges at these interfaces creates internal potential barriers, highlighting the dominant role of grain boundary effects in the dielectric response. Such behavior is characteristic of materials with electrical heterogeneity, where localized charge carriers become thermally activated and contribute to interfacial polarization.[48] This leads to enhanced dielectric permittivity, especially in the low-frequency regime.

The elevated ε' values are attributed to various polarization mechanisms, including electronic, ionic, dipolar, atomic, and

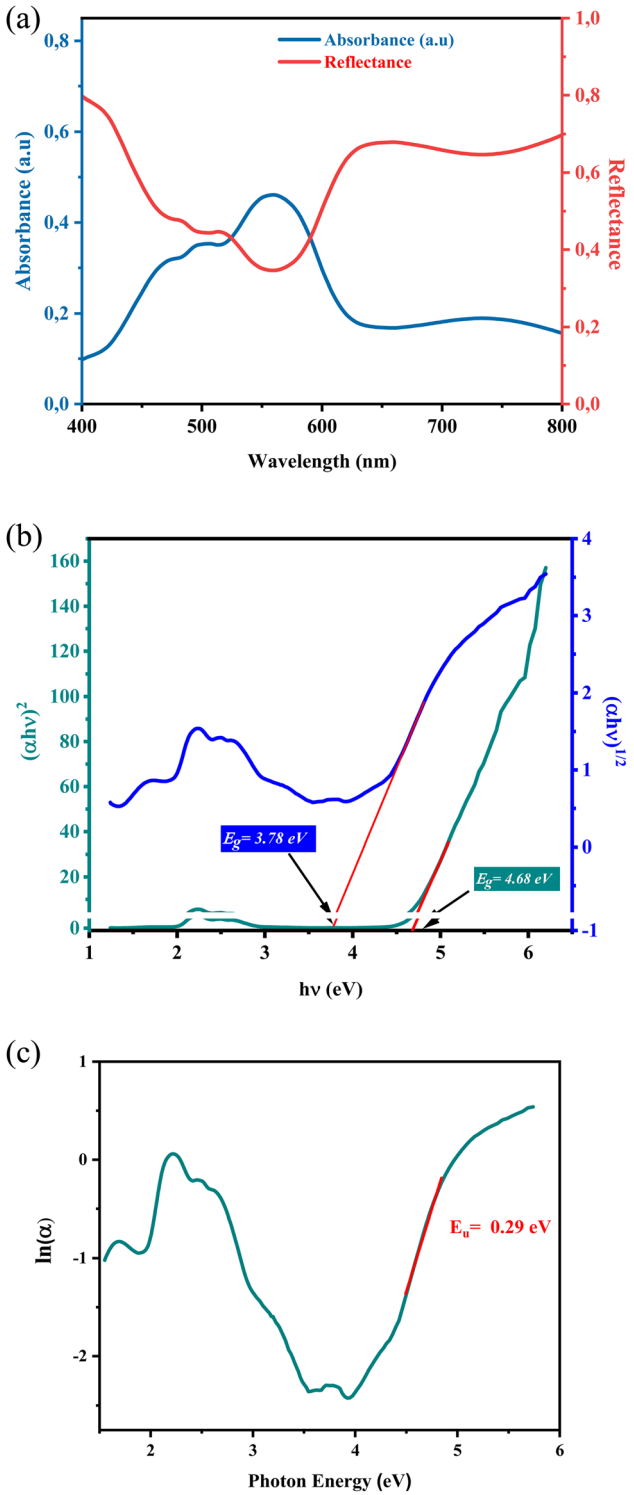

Fig. 6 (a) The UV-visible absorbance spectrum. (b) Direct and indirect band gap. (c) Ln(α) as a function of photon energy (eV) for $Li_2CoP_2O_7$ sample.

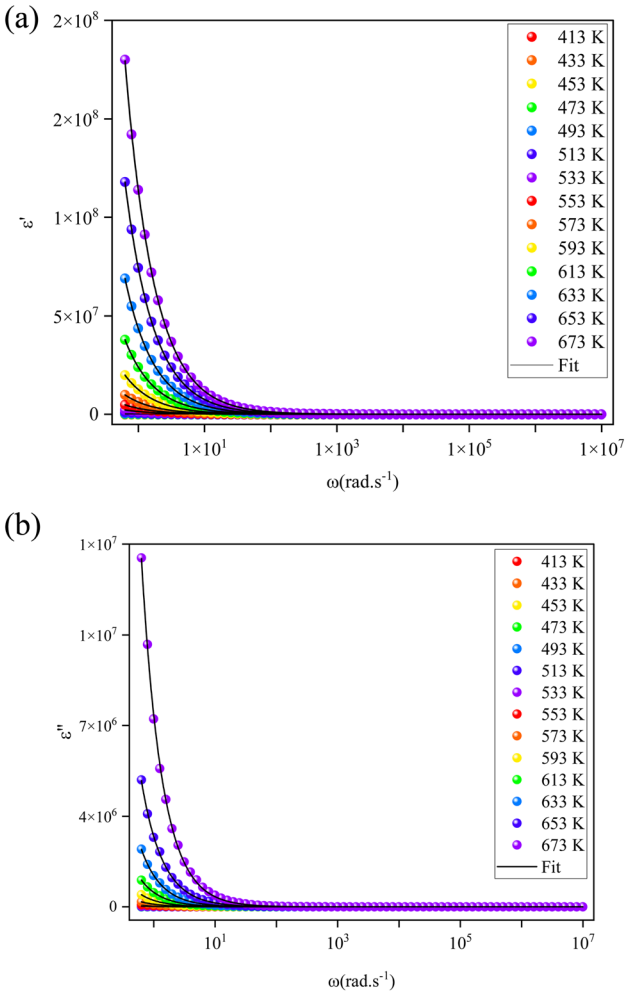

Fig. 7 (a) Frequency-dependent of real part of dielectric constants (ε') of $Li_2CoP_2O_7$. (b) Imaginary part (ε''), at different temperature of $Li_2CoP_2O_7$.

interfacial contributions.[49] In particular, the hopping of localized charge carriers and their trapping at structural interfaces contribute significantly to the observed dielectric enhancement.

As frequency increases, ε' decreases and eventually reaches a saturation level, forming a frequency-independent dielectric plateau. This reduction results from the inability of space charges to follow the rapidly oscillating external field, thereby reducing their influence on the dielectric response.[50] The position of this plateau shifts toward higher frequencies with increasing temperature, consistent with thermally activated relaxation processes.

These results underscore the importance of microstructural features such as grain size, grain boundary density, and porosity in governing the dielectric behavior. Fine-grained ceramics typically exhibit higher dielectric constants due to enhanced interfacial polarization. Conversely, the presence of voids can reduce dielectric performance by lowering density and increasing resistivity. Overall, the high permittivity and frequency-dependent behavior suggest that $Li_2CoP_2O_7$ is a promising material for low-frequency energy storage and electronic applications,[51] comparable to other phosphate-based dielectrics like $Li_2NiP_2O_7$ and $Ag_2CrP_2O_7$.[52]

Fig. 7(b) displays the frequency-dependent variation of the imaginary part of the dielectric permittivity (ε'') for $Li_2CoP_2O_7$ over the temperature range of 413–673 K. This parameter provides insight into the energy dissipation mechanisms within the material matrix.[53] The ε'' component reflects dielectric losses associated with processes such as dipolar relaxation, charge transport, and interfacial polarization phenomena.[54] One of the primary contributors to this behavior is space charge redistribution, which is significantly influenced by structural defects and grain boundary resistivity. At low frequencies, mobile charge carriers can accumulate at grain boundaries, leading to pronounced interfacial polarization effects.[55] This accumulation enhances dielectric losses, as evidenced by the elevated ε'' values in this region, indicating substantial energy dissipation. The observed increase in ε'' at low frequencies is therefore primarily attributed to the barrier effects at grain boundaries that restrict charge mobility between neighboring conductive grains. Consequently, greater energy is required for charge transport across these interfaces. As frequency increases, the influence of grain boundary impedance diminishes, and a decline in ε'' is observed. This reduction corresponds to a transition toward hopping conduction mechanisms, where charge carriers experience fewer interfacial constraints and instead engage in localized or extended hopping between sites.[56] Below the characteristic relaxation frequency, ε'' increases with temperature, reflecting a higher density of thermally activated charge carriers involved in the conduction process.[57] In contrast, at higher frequencies, where intragranular dynamics dominate, ε'' tends to decrease with increasing temperature, likely due to a decline in the population of free charge carriers. This behavior can be ascribed to energy losses stemming from Li^+ ion migration, dipole reorientation, and polarization relaxation effects.

3.6. Study of electrical conductivity

In this section, the electrical properties of the synthesized $Li_2CoP_2O_7$ pyrophosphate were investigated through conductivity measurements and theoretical modeling, offering insights into the underlying charge transport mechanisms within the material.[58] The AC conductivity was examined across a broad frequency range (10^{-1} to 1×10^7 Hz) and a temperature interval from 413 K to 673 K.

Fig. 8 presents the frequency-dependent conductivity (σ) spectra recorded at various temperatures. A clear increase in conductivity with rising temperature is observed, indicating thermally activated conduction processes. The spectra can be interpreted in two distinct frequency regimes. At low frequencies (up to $\sim 10^3$ Hz), a plateau region is evident, corresponding to the DC conductivity (σ_{dc}), which increases with temperature. At higher frequencies (above $\sim 10^3$ Hz), a dispersive region appears where the conductivity becomes increasingly dependent on frequency, representing the AC conductivity (σ_{ac}). This dispersion suggests enhanced carrier mobility due to thermally activated hopping mechanisms (Fig. 9).

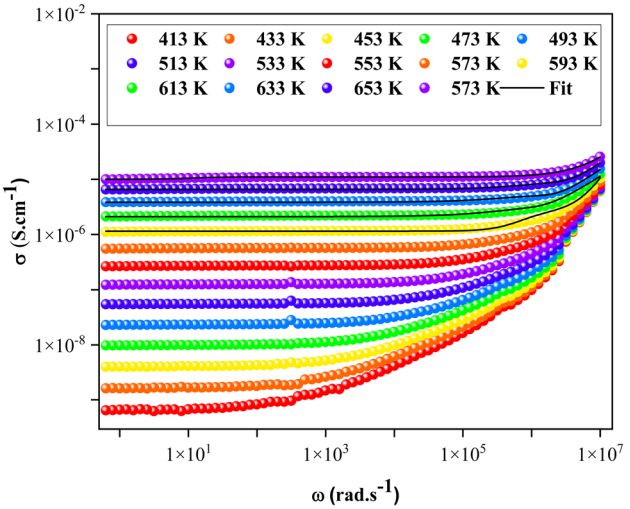

Fig. 8 The variation of $\ln(\sigma_{ac})$ *versus* $\ln(\omega)$ at different temperatures of $Li_2CoP_2O_7$.

The overall behavior of the conductivity spectra at all temperatures is well described by the empirical Jonscher's universal power law,[59] confirming the contribution of localized charge carrier dynamics.

$$\sigma_{ac} = \sigma_{dc} + A\omega^s \quad (10)$$

The first term represents the contribution of DC electrical conductivity in the compound, while the second term is introduced to analyze the material's response in the dynamic (AC) region of the spectra. In this context, the frequency exponent "*s*" plays a crucial role by characterizing the interaction strength between mobile charge carriers and shedding light on the underlying conduction mechanisms. Various theoretical models have been proposed to explain the

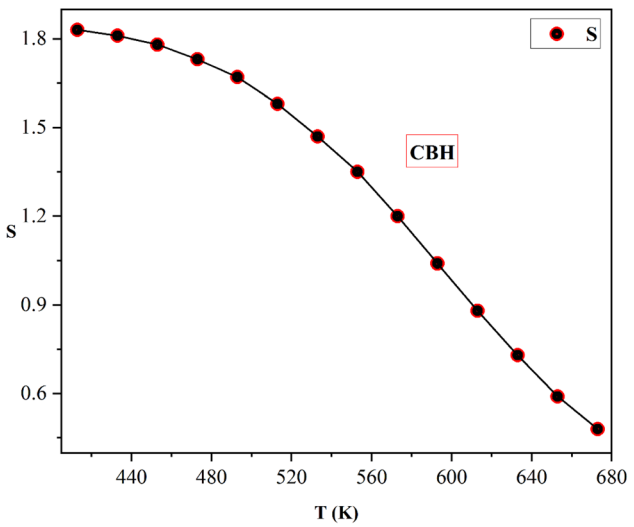

Fig. 9 Temperature dependence of the exponent "s" of the sample prepared.

temperature dependence of $s(T)$ and its correlation with AC conductivity. According to the Overlapping Large Polaron Tunneling (OLPT) model, the exponent s decreases with increasing temperature until reaching a minimum, beyond which it begins to increase.[60] In contrast, the Non-Overlapping Small Polaron Tunneling (NSPT) model suggests a monotonic increase of s with temperature.[61] The Correlated Barrier Hopping (CBH) model predicts a consistent decrease in s as temperature rises.[62] Meanwhile, the Quantum Mechanical Tunneling (QMT) model indicates that s remains nearly constant or shows a slight increase, typically approaching a value around 0.8, which aligns well with experimental observations.[63]

Fig. 12 illustrates the temperature-dependent behavior of the frequency exponent s for the $Li_2CoP_2O_7$ compound. As the temperature increases from 413 K to 673 K, a noticeable decline in the value of s is observed. This inverse relationship between s and temperature is indicative of a thermally activated conduction process. Such a trend is characteristic of the Correlated Barrier Hopping (CBH) model, which describes charge transport in disordered materials. In this framework, the conduction arises from the thermally assisted hopping of charge carriers between localized states over potential barriers. The decreasing trend of s with rising temperature supports the notion that, at elevated temperatures, the energy barriers become easier to overcome, facilitating more efficient hopping and thereby reducing the frequency dependence of the AC conductivity. In relation to this model, the exponent (s) can be determined using the following equation:[64]

$$s = 1 - \frac{6K_B T}{W_m + K_B T \ln(\omega\tau_0)} \quad (11)$$

In this context, W_m represents the binding energy required for transferring an electron between sites, T is the absolute temperature, and τ_0 denotes the characteristic relaxation time. The results demonstrate that the chosen model effectively predicts the electrical properties of materials across various temperatures, offering substantial potential for numerous technological applications.[65]

Fig. 10 illustrates the temperature dependence of conductivity by plotting $\ln(\sigma_{dc}\cdot T)$ against $1000/T$, revealing a linear increase in $\ln(\sigma_{dc}\cdot T)$ with rising temperature. This suggests that the conduction in the compound adheres to the Arrhenius law:[66]

$$\sigma_{dc} T = A \exp\left(-\frac{E_a}{k_B T}\right) \quad (12)$$

In this context, A represents the pre-exponential factor, E_a denotes the activation energy, k_B is the Boltzmann constant, and T signifies the absolute temperature.

The activation energy for charge transport, derived from a linear fit, is approximately 0.95 eV. This value aligns well with those observed in other semiconductor compounds containing diphosphates.[67] Additionally, it is comparable to the activation energy associated with the grain, suggesting that the overall conductivity is predominantly influenced by grain.

3.7. Complex electric modulus studies

The electric impedance and modulus are a crucial parameter for understanding the relaxation behavior of electric fields in materials under constant dielectric displacement.

Fig. 11(a) presents the frequency-dependent behavior of the imaginary part of the complex impedance (Z'') at various temperatures. Each spectrum displays a well-defined peak (Z_{max}''), which becomes broader and shifts toward higher frequencies with increasing temperature. This behavior indicates a thermally activated relaxation mechanism and suggests the presence of a distribution of relaxation times within the $Li_2CoP_2O_7$ pyrophosphate system.[68] The convergence of Z'' values at higher frequencies is likely due to a decrease in space charge effects, associated with the reduced potential barriers for charge transport at elevated temperatures. Additionally, this convergence may be influenced by the accumulation of charge carriers at interfacial regions, which becomes more prominent at high frequencies and contributes to enhanced AC conductivity. In the $Li_2CoP_2O_7$ lattice, such interfacial effects may stem from limited charge mobility, carrier trapping, or interactions at grain boundaries, all of which strongly influence the overall impedance response and facilitate the merging of Z'' profiles at higher frequencies.

Fig. 11(a) presents the frequency-dependent behavior of the imaginary part of the complex impedance (Z'') at various temperatures. Each spectrum displays a well-defined peak (Z_{max}''), which becomes broader and shifts toward higher frequencies with increasing temperature. This behavior indicates a thermally activated relaxation mechanism and suggests the presence of a distribution of relaxation times within the $Li_2CoP_2O_7$ pyrophosphate system.[69] The convergence of Z'' values at higher frequencies is likely due to a decrease in space charge effects, associated with the reduced potential barriers for charge transport at elevated temperatures. Additionally, this convergence may be influenced by the accumulation of

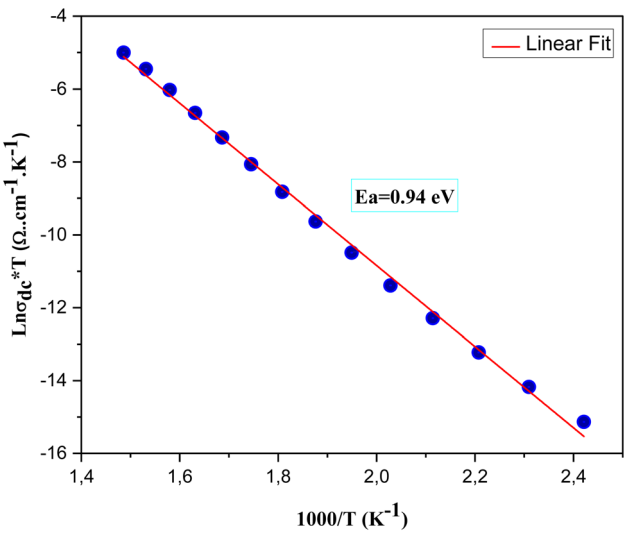

Fig. 10 Evolution of $\ln(\sigma_{dc} \times T)$ as a function of $(1000/T)$.

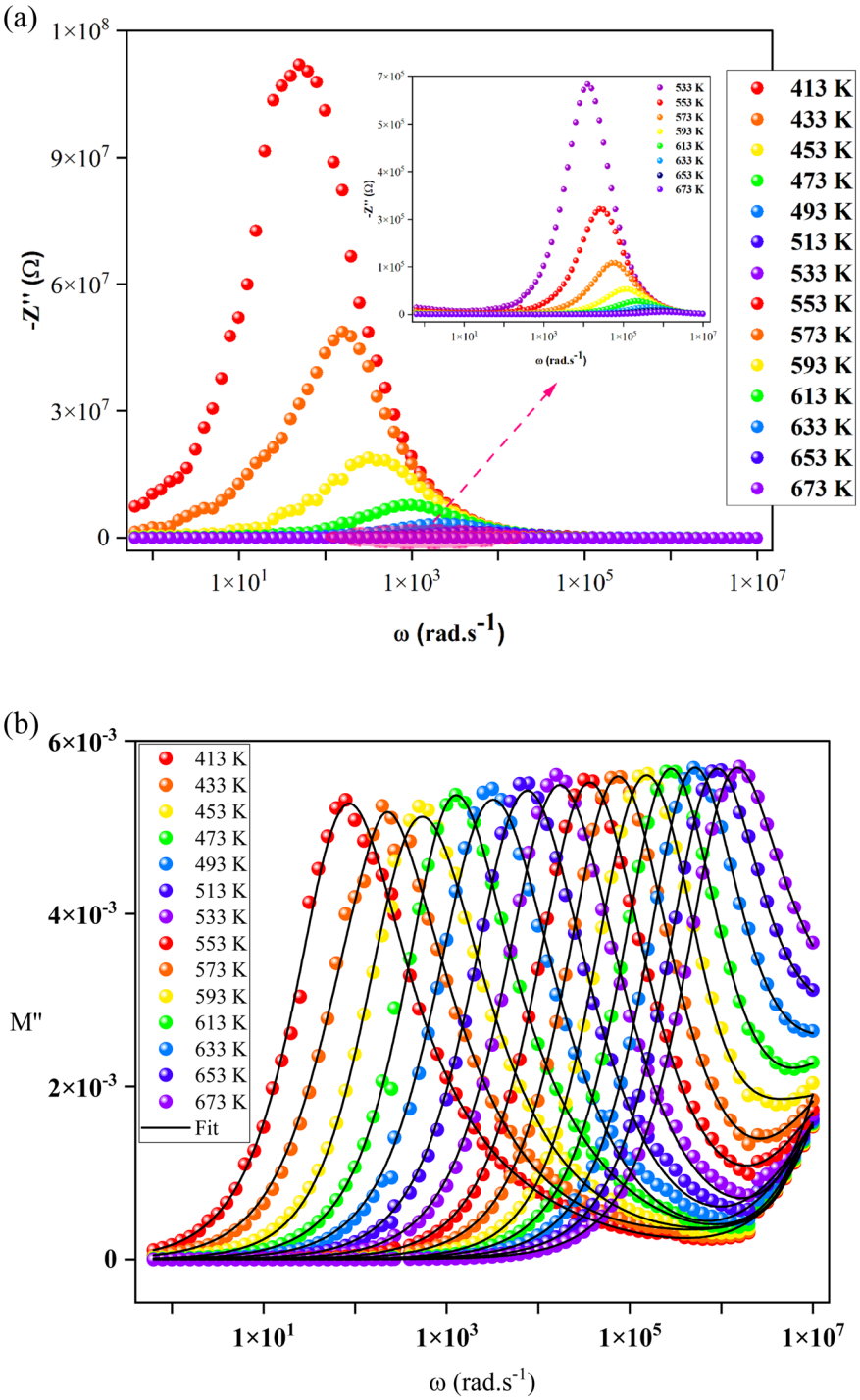

Fig. 11 (a) Frequency dependence of the imaginary part of electric impedance at different temperatures. (b) Frequency dependence of the imaginary part of electric modulus at different temperatures.

charge carriers at interfacial regions, which becomes more prominent at high frequencies and contributes to enhanced AC conductivity. In the $Li_2CoP_2O_7$ lattice, such interfacial effects may stem from limited charge mobility, carrier trapping, or interactions at grain boundaries, all of which strongly influence the overall impedance response and facilitate the merging of Z'' profiles at higher frequencies.

In ionic-conducting materials, the frequency-dependent characteristics of M'' can be interpreted through the Kohlrausch–Williams–Watts (KWW) model.[70]

The characteristic angular frequency of relaxation, denoted as ω_p, was determined from the peak positions observed in the $M''(\omega)$ spectra at various temperatures. To further investigate the relaxation dynamics, the activation energy (E_a) associated

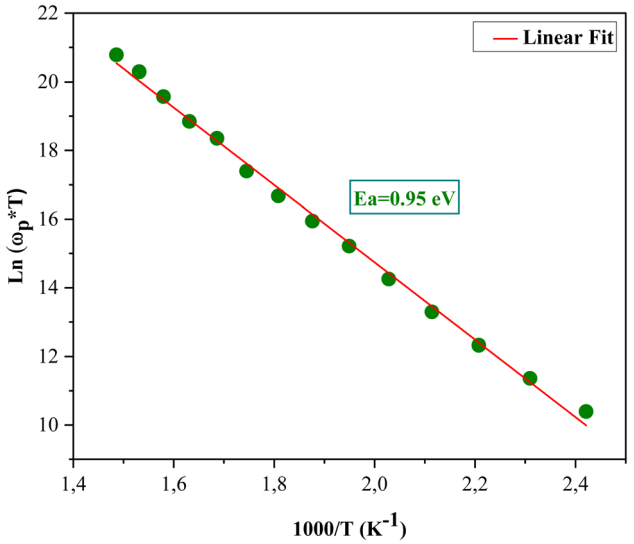

Fig. 12 Dependence of $\ln(\omega_p)$ *versus* reciprocal temperature for $Li_2CoP_2O_7$.

with this process was extracted using an Arrhenius-type analysis. Specifically, a plot of $\ln(\omega_p \times T)$ as a function of $1000/T$ (as shown in Fig. 12) was constructed. This linear relationship follows the Arrhenius equation given by:[71]

$$\omega_p = \frac{\omega_0}{T} \exp\left(\frac{-E_a}{K_B \times T}\right) \quad (13)$$

where ω_0 is the pre-exponential factor and is the k_B Boltzmann constant. The slope of this linear plot yielded an activation energy of approximately 0.95 eV. The obtained value is in good agreement with that derived from the analysis of DC conductivity, indicating that both relaxation and conduction processes are governed by similar thermally activated mechanisms. This consistency supports the conclusion that charge carrier motion plays a central role in the relaxation dynamics of the $Li_2CoP_2O_7$ system.[72]

Under the specified conditions, the appearance of a single peak introduces ambiguity in distinguishing the origin of the relaxation whether it is associated with grain or grain boundary contributions. This uncertainty limits the ability to deduce microstructural features based solely on relaxation frequencies or peak positions. To overcome this limitation, a comparative analysis of the imaginary parts of the impedance (Z'') and the electric modulus (M'') offers a more reliable approach. This combined method provides a broader and more insightful understanding of the relaxation mechanisms than evaluating either function independently. Accordingly, Fig. 13 presents the normalized spectra of M'' and Z'' at a corrected and representative temperature.

The Z'' spectrum exhibits a peak attributed to the grain response, while the M'' spectrum reveals a non-Debye relaxation peak at a different frequency. This divergence in peak positions indicates that charge carrier motion is confined to short-range hopping. In contrast, when both peaks coincide in frequency, it typically reflects long-range conduction processes.[73] Therefore, the frequency separation observed in our measurements suggests that the dominant transport mechanism in the studied material involves localized, short-range motion of charge carriers.[74]

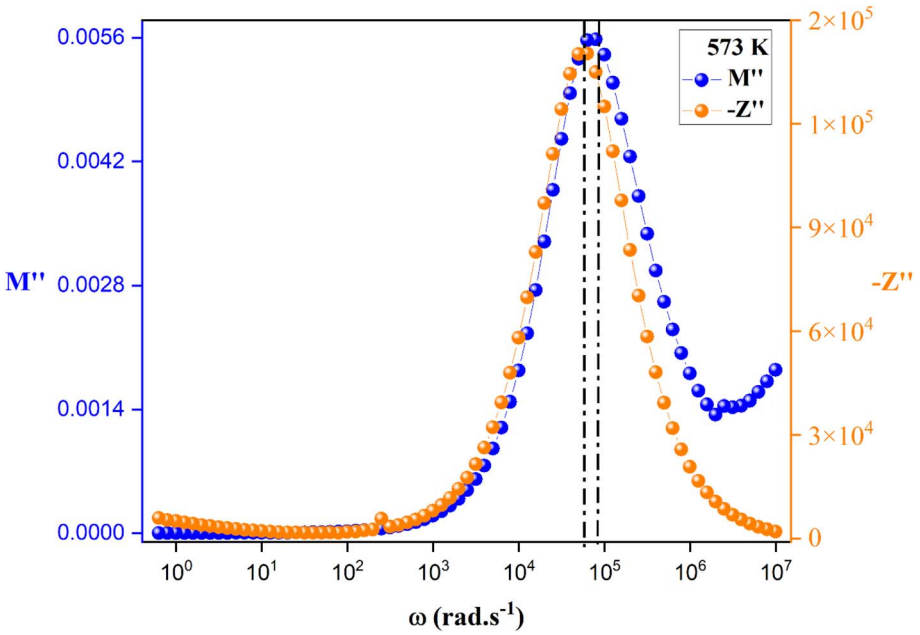

Fig. 13 Combined M'' and $-Z''$ spectroscopic plots.

4. Conclusion

In summary, $Li_2CoP_2O_7$ was successfully synthesized using the solid-state method. X-ray diffraction (XRD) confirmed that the sample is a single-phase compound, free of secondary phases, and crystallizes in the monoclinic $C2/c$ space group. Scanning Electron Microscopy (SEM) coupled with EDX confirmed the homogeneous distribution of elements and high purity. UV-visible spectroscopy revealed a indirect optical band gap of approximately 3.78 eV and an Urbach energy of 0.29 eV, indicating low structural disorder. The refractive index and dispersion parameters further highlight its potential for opto-electronic applications. Dielectric studies showed a high relative permittivity (ε') across the temperature range, confirming suitability for energy storage. AC conductivity analysis revealed frequency-dependent behavior well described by the Correlated Barrier Hopping (CBH) model, with a consistent conduction mechanism and activation energy values of ~0.95 eV (dc conductivity) and 0.94 eV (modulus analysis), indicating thermally activated transport. These results collectively demonstrate that $Li_2CoP_2O_7$ exhibits promising structural, optical, dielectric and electrical characteristics, positioning it as a potential candidate for next-generation dielectric and opto-electronic applications. This study lays a solid foundation for further research into diphosphate-based materials for advanced functional devices.[75,76]

Data availability

Data will be made available on request.

Author contributions

Samia Aydi: Writing– original draft, validation, software, methodology, investigation. Amar Djemli: Writing review & editing, writing– original draft, validation, methodology. Obaidallah A. Algethami: Writing– review & editing, validation, software, methodology. Sami Znaidia: Writing– original draft, visualization, formal analysis. Foudil Sahnoune: Writing– review & editing, writing– original draft, supervision, investigation. Abderrazek Oueslati: Writing– review & editing, visualization, validation, investigation, formal analysis, data curation.

Conflicts of interest

The authors declare that they have no known competing financial interests or personal relationships that could have appeared to influence the work reported in this paper.

Acknowledgements

The authors extend their appreciation to the Deanship of Research and Graduate Studies at King Khalid University for funding this work through Large Research Project under grant number RGP2/240/46.

References

1 S. P. Ong, V. L. Chevrier, G. Hautier, A. Jain, C. Moore, S. Kim, X. Ma and G. Ceder, *Energy Environ. Sci.*, 2011, **4**, 3680.
2 S. Kim, X. Ma, S. P. Ong and G. Ceder, *Phys. Chem. Chem. Phys.*, 2012, **14**, 15571.
3 G. Shao, D. A. H. Hanaor, J. Wang, D. Kober, S. Li, X. Wang, X. Shen, M. F. Bekheet and A. Gurlo, *ACS Appl. Mater. Interfaces*, 2020, **12**, 46045.
4 M. M. Thackeray, J. O. Thomas and M. S. Whittingham, *MRS Bull.*, 2000, **25**, 39.
5 J. Xu, F. Lin, M. M. Doeff and W. Tong, *Mater. Chem.*, 2017, **A 5**, 874.
6 N. A. Chernova, M. F. V. Hidalgo, C. Kaplan, K. Lee, I. Buyuker, C. Siu, B. Wen, J. Ding, M. Zuba, K. M. Wiaderek, L. D. Seymour, S. Britto, L. F. J. Piper, S. P. Ong, K. W. Chapman, C. P. Grey and M. S. Whittingham, *Adv. Energy Mater.*, 2020, **10**, 2002638.
7 W. Du, Z. Zhang, Z. Chen and J. Li, *Phys. Status Solidi B*, 2021, 2000420.
8 J. Ling, C. Karuppiah, S. G. Krishnan, M. V. Reddy, I. I. Misnon, M. H. A. Rahim, C.-C. Yang and R. Jose, *Energy Fuel.*, 2021, **35**, 10428.
9 L. Sharma, S. P. Adiga, H. N. Alshareef and P. Barpanda, *Adv. Energy Mater.*, 2020, **10**, 2001449.
10 G. Rousse and J. M. Tarascon, *Chem. Mater.*, 2014, **26**, 394.
11 L. Spitthoff, P. R. Shearing and O. S. Burheim, *Energies*, 2021, **14**, 1248.
12 A. K. Padhi, K. S. Nanjundaswamy and J. B. Goodenough, *Electrochem. Soc.*, 1997, **144**, 1188.
13 I. Sadaba, S. Lima and A. A. Valente, *Carbohydr. Res.*, 2011, **346**, 2785.
14 H. Fukuoka, H. Matsunaga and S. Yamanaka, *Mater. Res. Bull.*, 2003, **38**, 991.
15 S. Nishimura, N. Nakamura, R. Natsui and A. Yamada, *Am. Chem. Soc.*, 2010, **132**, 13596.
16 A. Sengupta, A. Chamuah, R. Ram, C. K. Ghosh, S. Diyali, B. Biswas, M. S. Ali and S. Bhattacharya, *ECS J. Solid State Sci. Technol.*, 2022, **11**, 113008.
17 O. Ajili, B. Louati and K. Guidara, *Indian J. Phys.*, 2018, **92**, 875.
18 N. Khay and A. Ennaciri, *Raman Spectrosc.*, 2001, **32**, 1052.
19 H. Ye, C. Q. Sun and H. Huang, *Thin Solid Films*, 2001, **381**, 52.
20 A. Oueslati, *Ionics*, 2017, **23**, 857.
21 M. Sassi, A. Oueslati, N. Moutia, K. Khirouni and M. Gargouri, *Ionics*, 2017, **23**, 847.
22 S. Afyon, M. Worle and R. Nesper, *Angew. Chem.*, 2013, **125**, 12773.
23 A. Nyten, A. Abouimrane, M. Armand, T. Gustafsson and J. O. Thomas, *Electrochem. Commun.*, 2005, **7**, 156.
24 W. Yao, A. R. Armstrong, X. Zhou, M.-T. Sougrati, P. Kidkhunthod, S. Tunmee, C. Sun, S. Sattayaporn, P. Lightfoot, B. Ji, C. Jiang, N. Wu, Y. Tang and H.-M. Cheng, *Nat. Commun.*, 2019, **10**, 3483.

25 Q. Ni, L. Zheng, Y. Bai, T. Liu, H. Ren, H. Xu, C. Wu and J. Lu, *ACS Energy Lett.*, 2020, **5**, 1763.
26 S. Zhou, T. Mei, X. Wang and Y. Qian, *Nanoscale*, 2018, **10**, 17435.
27 A. Chakraborty, S. Kunnikuruvan, S. Kumar, B. Markovsky, D. Aurbach and M. Dixit, *Chem. Mater.*, 2020, **32**, 915.
28 M. Takahashi, S.-I. Tobishima, K. Takei and Y. batteries, *Solid State Ionics*, 2002, **148**, 283.
29 K. T. Kozawa, A. Kondo, K. Fukuyama, M. Naito, H. Koga, Y. Shimo, T. Saito, H. Iba, Y. Inda, T. Oono, T. Katoh and K. Nakajima, *Solid State Electrochem.*, 2019, **23**, 1297.
30 K. Vijaya Babu, L. Seeta Devi, V. Veeraiah and K. Anand, *J. Australas. Ceram. Soc.*, 2016, **4**, 269.
31 N. V. Kosova, O. A. Podgornova, E. T. Devyatkina, V. R. Podugolnikov, S. A. Petrov and N. V. Kosova, *Mater. Chem.*, 2014, **A 2**, 20697.
32 S. Y. Chung, J. T. Bloking and Y. M. Chiang, *Nat. Mater.*, 2002, **1**, 123.
33 D. Mori, H. Kobayashi, T. Okumura, H. Nitani, M. Ogawa and Y. Inaguma, *Solid State Ionics*, 2016, **285**, 66.
34 Y. Lyu, E. Hu, D. Xiao, Y. Wang, X. Yu, G. Xu, S. N. Ehrlich, K. Amine, L. Gu, X.-Q. Yang and H. Li, *Chem. Mater.*, 2017, **29**, 9053.
35 M. Sathiya, K. Ramesha, G. Rousse, D. Foix, D. Gonbeau, A. S. Prakash, M. L. Doublet, K. Hemalatha and J. M. Tarascon, *Chem. Mater.*, 2013, **25**, 1121.
36 C. A. Schneider, W. S. Rasband and K. W. Eliceiri, NIH Image to Image J, *Nat. Methods*, 2012, **9**, 671.
37 E. Hu, Y. Lyu, H. L. Xin, J. Liu, L. Han, S.-M. Bak, J. Bai, X. Yu, H. Li and X.-Q. Yang, *Nano Lett.*, 2016, **16**, 5999.
38 D. Mori, H. Sakaebe, M. Shikano, H. Kojitani, K. Tatsumi and Y. Inaguma, *Power Sources*, 2011, **196**, 6934.
39 H. Zhou, S. Upreti, N. A. Chernova, G. Hautier, G. Ceder and M. S. Whittingham, *Chem. Mater.*, 2011, **23**, 293.
40 K. S. Nanjundaswamy, A. K. Padhi and J. B. Goodenough, *Solid State Ionics*, 1996, **92**, 1.
41 A. Ait-Salah, A. Mauger, K. Zaghib, J. B. Goodenough and N. Ravet, *J. Electrochem. Soc.*, 2006, **153**, A1692.
42 A. Ait-Salah, A. Mauger, C. M. Julien and F. Gendron, *Mater. Sci. Eng., B*, 2006, **129**, 232.
43 H. Kim, S. Lee, Y.-U. Park, H. Kim, J. Kim, S. Jeon and K. Kang, *Chem. Mater.*, 2011, **23**, 3930.
44 N. Shin-ichi, N. Megumi and N. Ryuichi, *J. Am. Chem. Soc.*, 2010, **132**, 13596.
45 H. Kim, S. Lee, Y. Park, H. Kim and J. Kim, *Chem. Mater.*, 2011, **23**, 3930.
46 Z. Jian, H. Yu and H. Zhou, *Electrochem. Commun.*, 2013, **34**, 215.
47 P. Pal and A. Ghosh, *Phys. Rev. Appl.*, 2020, **14**, 064010.
48 J. Liu, C. G. Duan, W. N. Mei, R. W. Smith and J. R. Hardy, *Appl. Phys.*, 2005, **98**, 093703.
49 N. H. Makani, A. Sahoo, P. Pal, T. Paul, L. S. Tanwar, M. Singh, A. Ghosh and R. Banerjee, *Phys. Rev. Mater.*, 2022, **6**, 115002.
50 C. R. Cena, A. K. Behera and B. Behera, *Adv. Ceram.*, 2016, **5**, 84.
51 C. G. Koops, *Phys. Rev.*, 1951, **83**, 121.
52 P. Sengupta, P. Sadhukhan, A. Ray, R. Ray, S. Bhattacharyya and S. Das, *Appl. Phys.*, 2020, **127**, 204103.
53 M. Ahmad, M. A. Rafiq, K. Rasool, Z. Imran and M. M. Hasan, *Appl. Phys.*, 2013, **113**, 043704.
54 D. K. Pradhan, P. Misra, V. S. Puli, S. Sahoo, D. K. Pradhan and R. S. Katiyar, *Appl. Phys.*, 2014, **115**, 243904.
55 R. Chen, Q. Li, X. Yu, L. Chen and H. Li, *Chem. Rev.*, 2019, **120**, 6820.
56 D. T. Hallinan, I. Villaluenga and N. P. Balsara, *MRS Bull.*, 2018, **43**, 759.
57 L. Long, *Mater. Chem.*, 2016, **A 4**, 10038.
58 Z. Zhang, Y. Shao, B. Lotsch, Y. S. Hu, H. Li, J. Janek, L. F. Nazar, C. W. Nan, J. Maier and M. Armand, *Energy Environ. Sci.*, 2018, **11**, 1945.
59 P. J. Lian, B. S. Hao, L. Q. Zhang, N. Xu, M. T. Wu and X. P. Gao, *Mater. Chem.*, 2019, **A 7**, 20540.
60 J. C. Bachman, S. Muy, A. Grimaud, H. H. Chang, N. Pour, S. F. Lux, O. Paschos, F. Maglia, S. Lupart and P. Lamp, *Chem. Rev.*, 2016, **116**, 140.
61 M. Hou, F. Liang, K. Chen, Y. Dai and D. Xue, *Nanotechnology*, 2020, **31**, 132003.
62 J. Dai, C. Yang, C. Wang, G. Pastel and L. Hu, *Adv. Mater.*, 2018, **30**, 1802068.
63 H. Aono, N. Imanaka and G. Adachi, *Acc. Chem. Res.*, 1994, **27**, 265.
64 H. Aono, E. Sugimoto, Y. Sadaoka, N. Imanaka and G. Y. Adachi, *Electrochem. Soc.*, 1990, **137**, 1023.
65 J. A. Dias, S. H. Santagneli and Y. Messaddeq, *J. Phys. Chem. C*, 2020, **124**, 26518.
66 N. Boaretto, I. Garbayo, S. Valiyaveettil-SobhanRaj, A. Quintela, C. Li, M. Casas- Cabanas and F. Aguesse, *Power Sources*, 2021, **502**, 229919.
67 Y. Moualhi, A. Mleiki, H. Rahmouni, K. Khirouni and A. Cheikhrouhou, *Mater. Res. Bull.*, 2022, **155**, 111976.
68 R. Cheruku, L. Vijayan and G. Govindaraj, *Mater. Sci. Eng., B*, 2012, **177**, 771.
69 S. Chkoundali, I. Garoui, W. Trigui and A. Oueslati, Crystal structure, *RSC Adv.*, 2024, **14**, 8971.
70 M. ben gzaiel, I. Garoui, F. N. Almutairi, I. Mbarek and O. A, *Opt. Mater.*, 2024, **154**, 115664.
71 M. Mnakri, I. Gharbi, M. Enneffati and A. Oueslati, *Mater. Today Commun.*, 2024, **38**, 107714.
72 S. Eom, P. Kavle, D. Kang, Y. Kim, L. W. Martin and S. Hong, *Adv. Funct. Mater.*, 2024, **35**, 2406944.
73 I. Gharbi, A. Ghoudi, I. Kammoun, A. Mahmoud and A. Oueslati, *Inorg. Chem. Commun.*, 2024, **166**, 112565.
74 I. Garoui, M. Mallek, F. N. Almutairi, W. Rekik and A. Oueslati, *J. Mol. Struct.*, 2024, **1315**, 138881.
75 M. B. Bechir, A. Almeshal and M. H. Dhaou, *Mater. Res. Bull.*, 2023, **157**, 112012.
76 A. Ghoudi, *et al*, *RSC Adv.*, 2023, **13**, 12844.